Journal of Materials Chemistry A

PAPER

View Article Online
View Journal | View Issue

Cite this: J. Mater. Chem. A, 2017, 5, 7618

Polymorphism in the family of $Ln_{6-x}MoO_{12-\delta}$ (Ln = La, Gd–Lu; $x = 0$, 0.5) oxygen ion- and proton-conducting materials

A. V. Shlyakhtina,*[a] S. N. Savvin,[b] N. V. Lyskov,[c] I. V. Kolbanev,[a] O. K. Karyagina,[d] S. A. Chernyak,[e] L. G. Shcherbakova[a] and P. Núñez[b]

Received 17th November 2016
Accepted 27th March 2017

DOI: 10.1039/c6ta09963g

rsc.li/materials-a

The formation of $Ln_{6-x}MoO_{12-\delta}$ (Ln = La, Gd, Dy, Ho, Er, Tm, Yb, Lu; $x = 0$, 0.5) rare-earth molybdates from mechanically activated oxide mixtures has been studied in the range 900–1600 °C. The morphotropy and polymorphism (thermodynamic phase and kinetic (growth-related) transitions) of the $Ln_{6-x}MoO_{12-\delta}$ (Ln = La, Gd–Lu; $x = 0$, 0.5) molybdates have been analyzed in detail. As a result we have observed two new types of oxygen ion- and proton-conducting materials with bixbyite ($Ia\bar{3}$, no. 206) and rhombohedral ($R\bar{3}$, no. 148) structures in the family of $Ln_{6-x}MoO_{12-\delta}$ (Ln = La, Gd–Lu; $x = 0$, 0.5) molybdates. The heavy rare-earth molybdates $Ln_{6-x}MoO_{12-\delta}$ (Ln = Er, Tm, Yb; $x = 0$, 0.5) have been shown for the first time to undergo an order–disorder (rhombohedral–bixbyite) phase transition at 1500–1600 °C, and we have obtained compounds and solid solutions with the bixbyite structure ($Ia\bar{3}$). The stability range of the rhombohedral phase ($R\bar{3}$) increases with decreasing Ln ionic radius across the $Ln_{6-x}MoO_{12-\delta}$ (Ln = Er, Tm, Yb, Lu) series. We have detected a proton contribution to the conductivity of the rhombohedral $La_{5.5}MoO_{11.25}$ (2×10^{-4} S cm^{-1} at 600 °C in wet air) and high-temperature polymorph $Yb_6MoO_{12-\delta}$ bixbyite structure, ($Ia\bar{3}$) below 600 °C. At these temperatures, rhombohedral ($R\bar{3}$) Yb_6MoO_{12} seems to be an oxygen ion conductor (E_a = 0.53–0.58 eV). The total conductivity of rhombohedral ($R\bar{3}$) Yb_6MoO_{12} exceeds that of bixbyite $Yb_6MoO_{12-\delta}$ by more than one order of magnitude and is 3×10^{-5} S cm^{-1} at 500 °C. According to their high-temperature (T > 600 °C) activation energies, the lanthanum and ytterbium molybdates studied here are mixed electron–ion conductors.

Introduction

Ln_6MoO_{12}, Ln_6WO_{12}, and solid solutions based on these compounds have recently been the subject of intense research as promising environmentally friendly dyes, luminescent materials, effective catalysts, and oxygen ion and proton conductors.[1–11] Tungstates and molybdates in these series are known to undergo various structural transformations with decreasing Ln ionic radius. The compounds in the Ln_6WO_{12} series have the fluorite structure ($Fm\bar{3}m$, no. 225) at Ln = La–Pr, a pseudotetragonal structure at Ln = Nd–Gd, and a rhombohedral structure ($R\bar{3}$, no. 148) at Ln = Tb–Lu. The Ln_6MoO_{12} series has a morphotropic phase transition from the fluorite structure at Ln = La–Ho to a rhombohedral structure ($R\bar{3}$) at Ln = Ho–Lu. It is also known that the molybdates exhibit a rich polymorphism, with polymorphic transformations between phases belonging to the fluorite series. In particular, both the $Fm\bar{3}m$ and $R\bar{3}$ polymorphs were obtained at high temperatures for the lanthanide molybdates with Ln = La–Sm and Ho, whereas among the tungstates only for Y_6WO_{12} the formation of an $R\bar{3}$ phase (above 1200 °C) and an $Fm\bar{3}m$ fluorite phase (at 1765 °C) was reported.[12] It may be that the relatively poor polymorphism of the tungstates is due to the extremely high temperatures of thermodynamic order–disorder transitions in Ln_2O_3–WO_3 systems. However especially for Ln_6WO_{12} (Ln = Y, La–Yb except Ce, Pm, Eu, Tb, Tm) the cubic high-temperature ($T_{syn.}$ > 1960 °C) bixbyite polymorph ($Ia\bar{3}$, no. 206) was reported by Foex.[13]

At the same time, a number of reports mention low-temperature cubic Ln_6MoO_{12} and Ln_6WO_{12} phases, which exist, as a rule, in the range 700–1000 °C and have rather broad diffraction lines. The formation of such low-temperature, poorly crystallized cubic phases was observed in the synthesis of compounds by various wet-chemical methods followed by annealing between 700 and 1000 °C. For example, a low temperature fluorite phase was observed in the synthesis of Y_6WO_{12} at 600 °C using a polymerized complex method.[14] A

[a]Semenov Institute of Chemical Physics, Russian Academy of Sciences, ul. Kosygina 4, Moscow, 119991, Russia. E-mail: annashl@inbox.ru; annash@chph.ras.ru
[b]Department of Inorganic Chemistry, Institute of Materials and Nanotechnology, University of La Laguna, Tenerife, La Laguna, 38200, Spain
[c]Institute of Problems of Chemical Physics, Russian Academy of Sciences, Academician Semenov ave. 1, Chernogolovka 142432, Moscow region, Russia
[d]Emanuel Institute of Biochemical Physics, Russian Academy of Sciences, ul. Kosygina 4, Moscow 119991, Russia
[e]Department of Chemistry, Lomonosov Moscow State University, 1–3 Leninskie Gory, Moscow, 119991, Russia

fluorite phase was detected in the range 800–1100 °C for Lu_6WO_{12} and 800–1000 °C for Lu_6MoO_{12} with the use of the citrate complexation method, followed by calcinations at these temperatures.[6] Recently, a low-temperature fluorite-like bixbyite polymorph ($Ia\bar{3}$) has been obtained using the solution combustion reaction between 700 and 1000 °C in Ln_6MoO_{12} (Ln = Tm, Yb, Lu).[15] In a study of the formation of Ln_6WO_{12} (Ln = Nd, Eu, Er) tungstates between 700 and 1480 °C using a sol–gel complexation synthesis method, Escolastico *et al.*[16] obtained low-temperature fluorites at temperatures from 700 to 1000 °C.

A distinction is made between thermodynamic phase transitions and kinetic (growth-related) order–disorder transitions. In the thermodynamic phase transitions, structural changes result from changes in thermodynamic conditions (pressure p and temperature T). The basic trends of structural changes caused by an increase in temperature or pressure were formulated by Goldschmidt:[17] the average coordination numbers (CNs) of atoms increase with increasing pressure and density and decrease with increasing temperature and decreasing density. High-temperature phases typically have higher symmetries than do low-temperature phases. In particular, many high-temperature phases have cubic structures, whereas low-temperature phases have lower symmetry. There are, however, exceptions. For example, the CN of one of the lanthanum atoms in La_2S_3 increases from 7 to 8 as a result of the α-La_2S_3 → γ-La_2S_3 phase transition at 1570 °C.[18]

There are also kinetic (growth-related) order–disorder transitions. These include the formation of a phase of a particular composition in the thermodynamic stability region of another phase with the same composition under the effect of kinetic factors such as crystal growth rate, particle attachment selectivity, *etc.*[19] This term was introduced by Chernov for describing the growth of a disordered crystal instead of an ordered, equilibrium crystal when slight differences in energy between sites become insignificant because of high growth rates.[20,21]

Solid solutions with a particular structure can result from kinetic ordering and disordering transitions.[19] Kinetic disordering transitions may be due to poor statistical selection of different atoms at high crystal growth rates (atoms in the surface layer do not have enough time to occupy sites corresponding to an ordered state before the formation of the next layer). The result is a disordered solid solution (typically with the fluorite structure according to X-ray diffraction (XRD) data). The formation of low-symmetry metastable phases (desymmetrization of crystals) in the case of ordered solid solutions is possible because the surface structure of a growing face differs significantly from the bulk structure of the crystal.

The kinetic (growth-related) order–disorder transitions considered above are characteristic of inorganic crystalline solid solutions.

Recently, kinetic (growth-related) metastable fluorite–pyrochlore (F*–P) transitions have also been classified with application to the pyrochlore family $Ln_2M_2O_7$ (Ln = La–Lu; M = Ti, Zr, Hf) oxygen-ion conductors.[22] The morphotropy and polymorphism (thermodynamic phase and kinetic (growth-related) transitions) of the $Ln_2M_2O_7$ (Ln = La–Lu; M = Ti, Zr, Hf) rare-earth pyrochlores have been analyzed in detail.[22,23]

The purpose of this work was to study the formation of rare-earth molybdate $Ln_{6-x}MoO_{12-\delta}$ (Ln = La, Gd, Dy, Ho, Er, Tm, Yb, Lu; $x = 0$, 0.5) solid solutions in a wide temperature range, from 900 to 1650 °C. To this end, precursors were synthesized using mechanical activation, a method that allows one to obtain homogeneous, highly dispersed oxide mixtures and occasionally leads to the formation of compounds at room temperature, *i.e.* ensures mechanochemical synthesis of mixed oxides.[24,25] Since a number of zirconium-doped rare-earth molybdates, $Ln_{5.4}Zr_{0.6}MoO_{12.3}$ (Ln = Nd, Sm, Dy) and $La_{5.8}Zr_{0.2}MoO_{12.1}$, were shown to possess oxygen ion and proton conductivity,[10,11] the total conductivity of some polymorphs of undoped $Ln_{6-x}MoO_{12-\delta}$ (Ln = La, Yb; $x = 0$, 0.5) was also measured in dry and wet air.

Experimental section

The $Ln_{6-x}MoO_{12-\delta}$ (Ln = La, Gd, Dy, Ho, Er, Tm, Yb, Lu; $x = 0$, 0.5) materials were prepared using the mechanical activation of starting oxides followed by high-temperature heat treatment of green compacts. All of the rare-earth oxides and molybdenum oxide used in our preparations were 99.9% pure.

After preheating the starting Ln_2O_3 (Ln = La, Gd, Dy, Ho, Er, Tm, Yb, Lu) oxides at 1000 °C for 2 h, they were mixed with MoO_3 and co-milled in a SPEX 8000 ball mill for 1 h. MoO_3 was previously activated in a high energy Aronov ball mill for 4 min. The mechanically activated mixtures of the oxides were uniaxially pressed at 680–914 MPa and sintered at 900, 1100, and 1200 °C for 4 h, and 1400, 1500 °C and 1600 °C for 3 h.

The geometric density of the as-prepared ceramics ranged from 64 to 96.38% of the theoretical one (Table 1). All samples were characterized structurally. X-ray diffraction (XRD) patterns of the polycrystalline samples were collected at room temperature on a DRON-3M automatic diffractometer (Cu Kα radiation, $\lambda = 1.5418$ Å, Bragg-reflection geometry, 35 kV, 28 mA) in the 2θ range 13° to 65° (scan step 0.1°). Table 1 summarizes the color, density, and crystallographic characteristics of the samples.

Energy dispersive X-ray spectroscopy (EDX) was realized by using a JEOL JSM-6390LA scanning electron microscope (SEM). An excitation energy of 20 keV was chosen as the accelerating voltage. The L-shells of Mo, La, Gd, Dy, Ho, Er, and Tm, and the M-shells of Yb and Lu were used for EDX analysis. 5–14 spectra were collected for each sample for Ln/Mo ratio determination. EDX measurements, as well as recording of the SEM images, were carried out in high vacuum mode (pressure $p \approx 4 \times 10^{-6}$ mbar). To prevent shifts in the images and heating of the sample caused by charging effects, the sample was coated with a 4 nm gold layer (Quorum Q150R ES) before the analysis. Microanalysis data of the Ln and Mo-containing samples are presented in Table 2.

The electrical conductivity of $Ln_{6-x}MoO_{12-\delta}$ (Ln = La, Yb; $x = 0$, 0.5) was characterized by two-probe AC impedance spectroscopy. Both faces of the disk-shaped polycrystalline samples sintered as described above (2–3 mm thick with a diameter of 9–10 mm) were covered with Pt ink (ChemPur C3605) and fired at 1000 °C for 30 min.

Table 1 Properties of the solid solutions

Sample no.	Composition	Synthesis temperature	Color	Relative density, %	Structure	Unit-cell parameters, Å
1	$La_{5.5}MoO_{11.25}$	900 °C-3 h	Grey	—	$Fm\bar{3}m$ (metastable)	$a = 5.478(1)$
2	$La_{5.5}MoO_{11.25}$	1600 °C-3 h	Dirty-yellow	91.1	Complex rhombohedral phase	
3	$Gd_6MoO_{12-\delta}$	1600 °C-3 h	Speckled yellow	90.05	$Fm\bar{3}m$ + traces of admixtures	$a = 5.382(3)$
4	$Gd_{5.5}MoO_{11.25-\delta}$	1500 °C-3 h	Speckled yellow	95.68	$Fm\bar{3}m$	$a = 5.378(2)$
5	$Gd_{5.5}MoO_{11.25-\delta}$	1600 °C-3 h	Speckled yellow	96.25	$Fm\bar{3}m$	$a = 5.379(1)$
6	$Dy_6MoO_{12-\delta}$	1500 °C-3 h	Speckled orange	84.32	$Fm\bar{3}m$ + traces of admixtures	$a = 5.312(2)$
7	$Dy_{5.5}MoO_{11.25-\delta}$	1500 °C-3 h	Speckled orange	92.86	$Fm\bar{3}m$	$a = 5.313(1)$
8	$Dy_{5.5}MoO_{11.25-\delta}$	1600 °C-3 h	Speckled brown	96.38	$Fm\bar{3}m$	$a = 5.313(1)$
9	$Ho_6MoO_{12-\delta}$	1400 °C-3 h	Yellow with separate spots	74.26	$Ia\bar{3}$	$a = 10.579(2)$
10	$Ho_6MoO_{12-\delta}$	1600 °C-3 h	Yellow with separate spots	85.2	$Ia\bar{3}$	$a = 10.583(4)$
11	$Ho_{5.5}MoO_{11.25-\delta}$	1400 °C-3 h	Speckled yellow	82.65	$Fm\bar{3}m$	$a = 5.292(3)$
12	$Ho_{5.5}MoO_{11.25-\delta}$	1500 °C-3 h	Speckled yellow	89.27	$Fm\bar{3}m$	$a = 5.291(2)$
13	$Ho_{5.5}MoO_{11.25-\delta}$	1600 °C-3 h	Speckled yellow	94.44	$Fm\bar{3}m$	$a = 5.291(2)$
14	Er_6MoO_{12}	1200 °C-40 h	Pink	—	$R\bar{3}$	$a = 9.695(4)$ $c = 9.242(4)$
15	Er_6MoO_{12}	1400 °C-3 h	Pink	78.76	$R\bar{3}$	$a = 9.697(4)$ $c = 9.249(6)$
16	$Er_6MoO_{12-\delta}$	1600 °C-3 h	Orange with separate spots	77.64	$Ia\bar{3}$	$a = 10.526(4)$
17	$Er_{5.5}MoO_{11.25-\delta}$	1600 °C-3 h	Speckled orange	96.25	$Fm\bar{3}m$	$a = 5.267(2)$
18	Tm_6MoO_{12}	1400 °C-3 h	Lemon	71.32	$R\bar{3}$	$a = 9.69(3)$ $c = 9.234(15)$
19	$Tm_6MoO_{12-\delta}$	1600 °C-3 h	Yellow with separate spots	76.58	$Ia\bar{3}$	$a = 10.474(14)$
20	Yb_6MoO_{12}	1200 °C-3 h	Lemon	65.86	$R\bar{3}$	$a = 9.614(2)$ $c = 9.170(2)$
21	Yb_6MoO_{12}	1400 °C-3 h	Lemon	75.06	$R\bar{3}$	$a = 9.610(2)$ $c = 9.169(2)$
22	Yb_6MoO_{12}	1500 °C-3 h	Lemon	78.12	$R\bar{3}$	$a = 9.612(2)$ $c = 9.166(2)$
23	$Yb_6MoO_{12-\delta}$	1600 °C-3 h	Yellow with separate spots	81.19	$Ia\bar{3}$	$a = 10.421(5)$
24	$Yb_{5.5}MoO_{11.25}$	1200 °C-3 h	Lemon	65.86	$R\bar{3}$	$a = 9.618(2)$ $c = 9.172(2)$
25	$Yb_{5.5}MoO_{11.25}$	1400 °C-3 h	Lemon	75.06	$R\bar{3}$	$a = 9.615(2)$ $c = 9.168(2)$
26	$Yb_{5.5}MoO_{11.25}$	1500 °C-3 h	Lemon	85.21	$R\bar{3}$	$a = 9.616(2)$ $c = 9.168(2)$
27	$Yb_{5.5}MoO_{11.25-\delta}$	1600 °C-3 h	Yellow with separate spots	87.2	$Ia\bar{3}$	$a = 10.439(6)$
28	Lu_6MoO_{12}	1400 °C-3 h	Lemon	64	$R\bar{3}$	$a = 9.594(6)$ $c = 9.127(4)$
29	Lu_6MoO_{12}	1600 °C-3 h	Light yellow	66.42	$R\bar{3}$	$a = 9.594(13)$ $c = 9.123(8)$

The temperature dependence of the total (electronic and ionic) conductivity of $La_{5.5}MoO_{11.25}$ in dry and wet air was extracted from impedance spectra obtained using a Solartron 1260 frequency response analyzer. The spectra were recorded in the frequency range of 0.1 Hz to 1 MHz on cooling from 900 °C to 150 °C; the root mean square ac voltage amplitude was set to 150 mV. Depending on the atmosphere and temperature it took from 2 to 5 h for the samples to reach the equilibrium conductivity values. The relative humidity of the air fed into the sample stage was controlled by passing it over freshly dehydrated silica gel (designated "dry") or through a water saturator maintained at 20 °C (designated "wet"), which ensured a constant water content of about 2%.

Electrical conductivity measurements of the two polymorphs, Yb_6MoO_{12} bixbyite ($Ia\bar{3}$) and Yb_6MoO_{12} rhombohedral ($R\bar{3}$), were performed using a P-5X potentiostat/galvanostat combined with a frequency response analyzer module (Elins Ltd, Russia) over the frequency range of 500 kHz to 0.1 Hz at a signal amplitude of 150 mV in the temperature range of 100–900 °C. A dry atmosphere was created by passing air through KOH and a wet atmosphere through a water saturator held at 20 °C. The air flow rate is 130 ml min^{-1}.

Results and discussion

Room-temperature synthesis of heavy rare-earth molybdate Yb_6MoO_{12} and intermediate rare-earth molybdate Ho_6MoO_{12} from oxides

Fig. 1a shows XRD patterns illustrating the mechanochemical synthesis of Yb_6MoO_{12} from its constituent oxides. Scan 1 in Fig. 1a represents the XRD pattern of unmilled Yb_2O_3, which has the bixbyite structure ($Ia\bar{3}$) (ICDD PDF 18-1463). Its lattice

Table 2 Microanalysis data of the samples under investigation

Sample no.	Composition	Synthesis temperature	Average nominal Ln/Mo atomic ratio	Average measured Ln/Mo atomic ratio
2	$La_{5.5}MoO_{11.25}$	1600 °C-3 h	5.5	5.7 ± 0.6
3	$Gd_6MoO_{12-\delta}$	1600 °C-3 h	6	6.5 ± 0.2
6	$Dy_6MoO_{12-\delta}$	1500 °C-3 h	6	6.4 ± 0.5
9	$Ho_6MoO_{12-\delta}$	1400 °C-3 h	6	6.5 ± 0.6
10	$Ho_6MoO_{12-\delta}$	1600 °C-3 h	6	6.3 ± 0.9
11	$Ho_{5.5}MoO_{11.25-\delta}$	1400 °C-3 h	5.5	6.1 ± 0.5
12	$Ho_{5.5}MoO_{11.25-\delta}$	1500 °C-3 h	5.5	5.5 ± 0.2
15	Er_6MoO_{12}	1400 °C-3 h	6	6.5 ± 0.5
16	$Er_6MoO_{12-\delta}$	1600 °C-3 h	6	6.3 ± 0.2
17	$Er_{5.5}MoO_{11.25-\delta}$	1600 °C-3 h	5.5	6.1 ± 0.3
19	$Tm_6MoO_{12-\delta}$	1600 °C-3 h	6	6.3 ± 0.4
21	Yb_6MoO_{12}	1400 °C-3 h	6	5.8 ± 0.2
23	$Yb_6MoO_{12-\delta}$	1600 °C-3 h	6	5.3 ± 0.4
A	$Er_{5.5}MoO_{11.25}$	1200 °C-40 h	5.5	6.6 ± 0.7
B	Tm_6MoO_{12}	1200 °C-40 h	6	6.6 ± 0.3

parameter was determined to be $a = 10.402(2)$ Å. Scans 2 and 3 in Fig. 1a represent XRD patterns of MoO_3 before and after grinding for 4 min in an Aronov vibrating ball mill. It is seen that the layered oxide MoO_3 readily amorphizes during grinding, and its lines become markedly broader. Also shown in Fig. 1a (scan 4) is the XRD pattern of a mixture of $3Yb_2O_3$ + MoO_3 (after 4 min of grinding (Aronov mill)). Since the mixture contains a considerable amount of ytterbium oxide, the relative amount of MoO_3 is not very large. After 40 min of subsequent grinding in a SPEX 8000 mill, we observed complete dissolution of the molybdenum oxide in Yb_2O_3 with the bixbyite structure ($Ia\bar{3}$). The resultant solid solution also had the bixbyite structure ($Ia\bar{3}$), and its lattice parameter was $a = 10.423(2)$ Å, *i.e.* it considerably exceeded that of the parent Yb_2O_3. Thus, it is reasonable to believe that an Yb_2O_3-based solid solution (Yb_6MoO_{12}) forms even during grinding, so this process can be thought of as the room-temperature mechanochemical synthesis of Yb_6MoO_{12} with the bixbyite structure ($Ia\bar{3}$). Note also that subsequent annealing at 1600 °C for 3 h had no significant effect on its lattice parameter $a = 10.421(5)$ Å (Table 1). A similar situation was observed for Tm_6MoO_{12} with parameter $a = 10.465(2)$ Å, which exceeded that of the parent Tm_2O_3 ($a = 10.459(1)$ Å).

Fig. 1b shows the XRD pattern of unmilled Ho_2O_3 with the bixbyite structure (($Ia\bar{3}$); $a = 10.583(2)$ Å) after annealing at 1000 °C for 1 h (scan 1) and the XRD patterns of MoO_3 before and after grinding for 4 min in the Aronov vibrating ball mill (scans 2 and 3). Also shown in Fig. 1b is the XRD pattern of a $3Ho_2O_3$ + MoO_3 mixture after 10 min of grinding in the SPEX mill (scan 4). It is seen that MoO_3 almost completely disappeared and that the reflections from Ho_2O_3 became markedly weaker and broader. Scans 5–7 in Fig. 1b represent the XRD patterns of the $3Ho_2O_3$ + MoO_3 mixture after 20, 40, and 60 min of grinding. It is seen that the superstructure reflections from the parent Ho_2O_3 (bixbyite structure, ($Ia\bar{3}$)) (Fig. 1b, scan 7) completely disappeared and that the strongest reflections remaining in the XRD pattern are due to a fluorite-like phase with $a = 5.301(2)$ Å and are markedly broadened.

Thus, the mechanochemical synthesis of heavy rare-earth molybdates (Yb_6MoO_{12}) differs from that of intermediate rare-earth molybdates (Ho_6MoO_{12}), which can be accounted for in terms of the nature of the starting oxide Ln_2O_3 (Ln = Yb, Ho).

$La_{6-x}MoO_{12-\delta}$ ($x = 0$, 0.5) formation from mechanically activated precursors

The ICDD PDF database of La_6MoO_{12} presents data on low-temperature phases, with broad diffraction lines,[26] whereas data on well-crystallized fluorite La_6MoO_{12} at high temperatures, $T \sim 1500$–1600 °C, are missing. Previously, rare-earth molybdates were studied as a rule at temperatures no higher than 1400 °C. However, the qualitative transpiration tests[27] indicated that the compounds R_6WO_{12} (R = Y, Tm, Lu) and Ln_6MoO_{12} (Ln = Tm–Lu) with a rhombohedral ($R\bar{3}$) structure demonstrate high thermal stability. After annealing for 2 h at 1750 °C in air, pellets of pure oxides, R_2O_3 (R = Y, Tm–Lu), had completely volatilized while both of the rhombohedral ($R\bar{3}$) Y_6MO_{12} (M = Mo, W) compounds showed only a small loss (0.1–0.3%) in weight.

Fig. 2 shows XRD patterns illustrating the phase formation process in $La_{5.5}MoO_{11.25}$ at 900, 1200, 1600, and 1650 °C (scans 1–4). When comparing the XRD patterns of $La_{5.5}MoO_{11.25}$ synthesized at 1600 and 1650 °C (Fig. 2, scans 3 and 4) to that of La_6MoO_{12} prepared at 1600 °C (Fig. 2, scan 5), it is important to note that, like La_6WO_{12},[8] La_6MoO_{12} does not exist as a distinct compound but is a mixture of $La_{6-x}MoO_{12-\delta}$ and La_2O_3 (ICDD PDF-2, no. 74-144) (*) as also are $La(OH)_3$ (ICDD PDF-2, no. 83-2034) (^), and $La_2O(CO_3)_2 \times H_2O$ (ICDD PDF-2, no. 28-512) (v), which are La_2O_3 hydration and carbonation products.

Given this, we synthesized not only Ln_6MoO_{12} but also $Ln_{5.5}MoO_{11.25}$ (Ln = La, Gd, Dy, Ho, Er, Yb) in order to prevent the final material from being multiphasic.

When analyzing the $La_{5.5}MoO_{11.25}$ formation process, it is worth noting the formation of a metastable, low-temperature fluorite phase at 900 °C, which then transforms into a rhombohedral ($R\bar{3}$) phase at 1200 °C (Fig. 2, scans 1 and 2). The

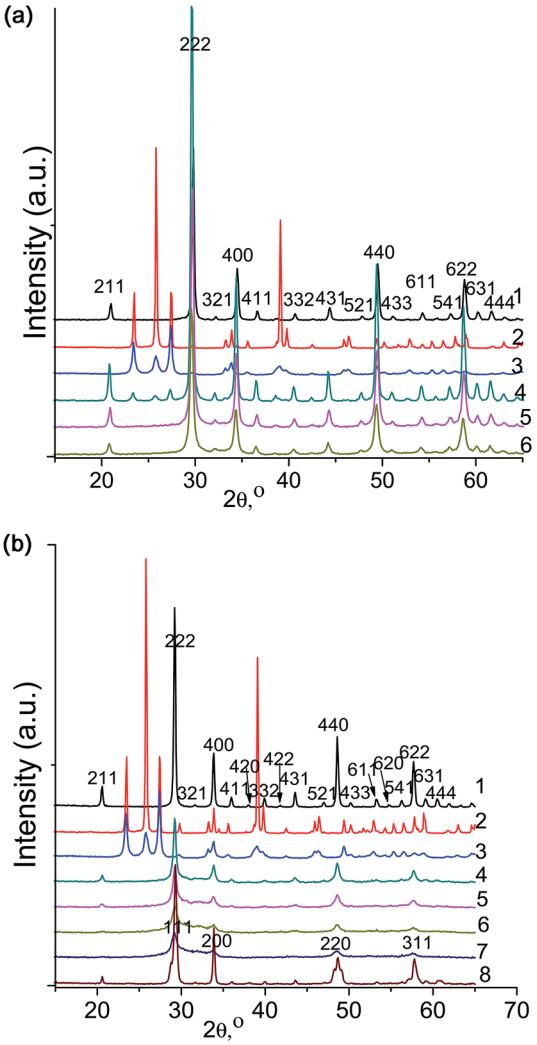

Fig. 1 (a) XRD patterns of (1) unmilled Yb_2O_3 with the bixbyite structure, (2) unmilled MoO_3, (3) MoO_3 after grinding for 4 min in an Aronov mill, (4) a $3Yb_2O_3$ + premilled MoO_3 (4 min) mixture, (5) the $3Yb_2O_3$ + premilled MoO_3 (4 min) mixture after grinding for 40 min in a SPEX 8000 mill, and (6) the $3Yb_2O_3$ + premilled MoO_3 (4 min) mixture after grinding for 60 min in the SPEX 8000; (b) XRD patterns of (1) unmilled Ho_2O_3 with the bixbyite structure after annealing at 1000 °C for 1 h, (2) unmilled MoO_3, (3) MoO_3 after grinding for 4 min in the Aronov mill, (4) a $3Ho_2O_3$ + premilled MoO_3 (4 min) mixture after grinding for 10 min in the SPEX 8000, (5) the $3Ho_2O_3$ + premilled MoO_3 (4 min) mixture after grinding for 20 min in the SPEX 8000, (6) the $3Ho_2O_3$ + premilled MoO_3 (4 min) mixture after grinding for 40 min in the SPEX 8000, (7) the $3Ho_2O_3$ + premilled MoO_3 (4 min) mixture after grinding for 60 min in the SPEX 8000, and (8) the $3Ho_2O_3$ + MoO_3 precursor (represented in scan 7) after heat treatment at 1100 °C for 4 h.

formation of a metastable, low-temperature fluorite phase was also observed in lutetium molybdate (Lu_6MoO_{12}) synthesis[6] and was reported for Y_6WO_{12} and Ln_6WO_{12} (Ln = Nd, Eu, Er, Lu) tungstates[14,16] prepared using wet-chemical methods and low temperature annealing at ~700–1000 °C.

Increasing the heat treatment temperature of $La_{5.5}MoO_{11.25}$ from 1200 to 1600 and 1650 °C led to the formation of a new phase that was also rhombohedral to a first approximation and had an increased unit-cell volume (increased unit-cell

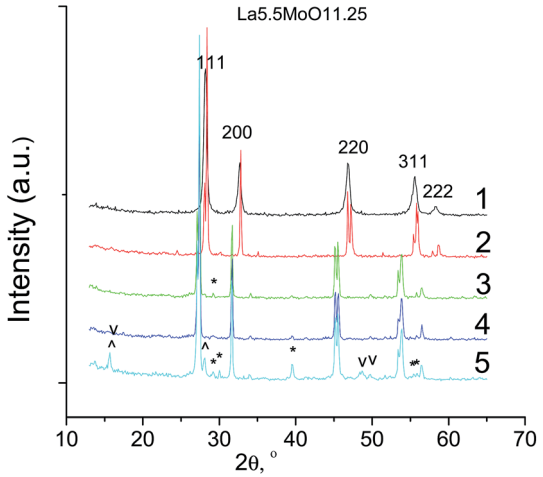

Fig. 2 XRD patterns, showing the process of phase formation of $La_{5.5}MoO_{11.25}$ from the mechanically activated oxide mixture under various conditions, (1) 900 °C-4 h, (2) 1200 °C-4 h, (3) 1600 °C-3 h, and (4) 1650 °C-3 h, in comparison with (5) La_6MoO_{12}, synthesized at 1600 °C-3 h. The XRD pattern of La_6MoO_{12} (curve 5) contains not only lines of La_2O_3 (ICDD PDF-2, no. 74-144) (*) but also those of $La(OH)_3$ (ICDD PDF-2, no. 83-2034) (^), and $La_2O(CO_3)_2 \times H_2O$ (ICDD PDF-2, no. 28-512) (v), which are La_2O_3 hydration and carbonation products.

parameter) (Fig. 2, scans 2–4). This phase was formed at 1600 °C and prevailed in multiphase La_6MoO_{12} (Fig. 2, scan 5). Comparison of XRD data of the zirconium-substituted molybdate $La_{5.8}Zr_{0.2}MoO_{12.1}$,[10] the $La_{5.5}MoO_{11.25}$ synthesized in this study, and a molybdenum-rich $La_{28-y}(W_{1-x}Mo_x)_{4+y}O_{54+\delta}$ tungstate[28] indicates that these solid solutions are identical in structure. Based on SAED results, Amsif *et al.*[28] proposed a rhombohedral cell with cells parameters (~28 × 28 × 9.8 Å), and with an unusually large volume of 6600 Å^3. Thus, further research is needed, with the use of neutron and synchrotron X-ray diffraction, to accurately determine the complex structure of $La_{5.5}MoO_{11.25}$.

$Gd_{6-x}MoO_{12-\delta}$ (x = 0, 0.5) formation from mechanically activated precursors

Fig. 3a and b show XRD patterns illustrating the phase formation process in Gd_6MoO_{12} and $Gd_{5.5}MoO_{11.25}$, respectively, at 900, 1200, 1500, and 1600 °C. For Gd_6MoO_{12} XRD of the sample after heat treatment at 1100 °C is presented also (Fig. 3a, scan 2). Heat treatment at 900 °C leads to the formation of a tetragonal phase (with all of its diffraction lines markedly broadened) (Fig. 3a and b, scans 1). A similar tetragonal phase was observed for Eu_6WO_{12} in the temperature interval 1200–1480 °C.[16] At 1200 °C, a tetragonal phase prevails (Fig. 3a and b, scans 3 and 2 respectively). At high temperatures, 1500–1600 °C, the $Gd_{5.5}MoO_{11.25-\delta}$ sample consists of a pure fluorite ($Fm\bar{3}m$) phase (Fig. 3b, scans 3 and 4), whereas the $Gd_6MoO_{12-\delta}$ sample contains impurity phases (Fig. 3a, scans 4 and 5). After annealing in the range 1500–1600 °C, the latter sample has a non-uniform coloration, with black inclusions. It seems likely that it is difficult to obtain impurity-free fluorite $Gd_6MoO_{12-\delta}$ by

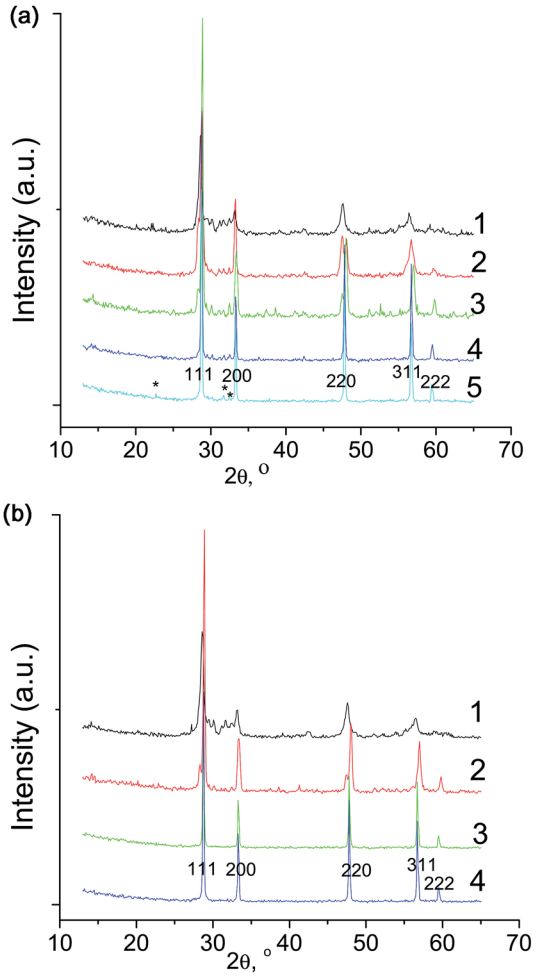

Fig. 3 (a) XRD patterns, demonstrating the process of phase formation of Gd_6MoO_{12} after heat treatment of the mechanically activated oxide mixture at the different temperatures: (1) 900 °C-4 h, (2) 1100 °C-4 h, (3) 1200 °C-3 h, (4) 1500 °C-3 h, and (5) 1600 °C-3 h. (b) XRD patterns, demonstrating the process of phase formation of $Gd_{5.5}MoO_{11.25}$ after heat treatment of the mechanically activated oxide mixture at the different temperatures: (1) 900 °C-4 h, (2) 1200 °C-3 h, (3) 1500 °C-3 h, and (4) 1600 °C-3 h.

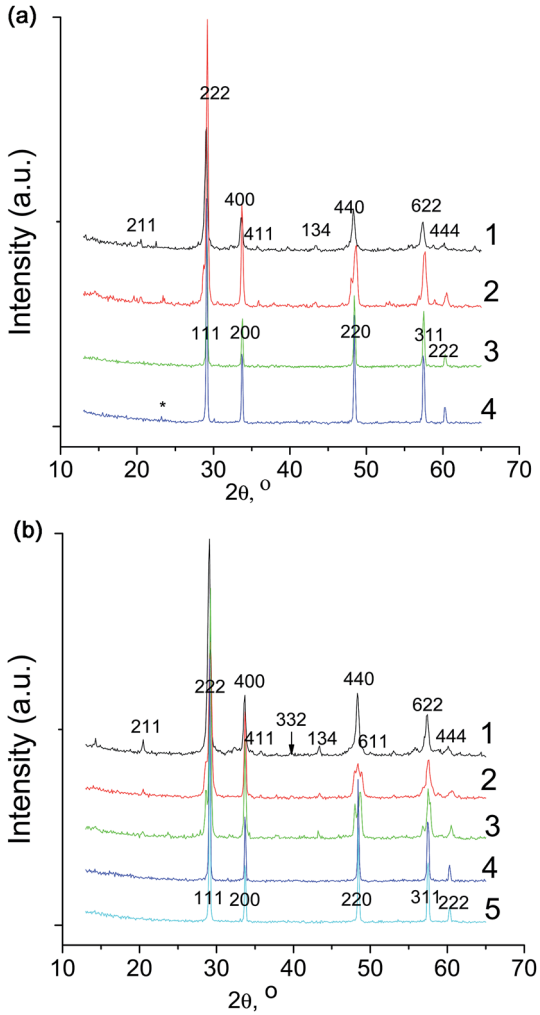

Fig. 4 (a) XRD patterns, showing the process of phase formation of Dy_6MoO_{12} after heat treatment of the mechanically activated oxide mixture under various conditions: (1) 900 °C-4 h, (2) 1200 °C-3 h, (3) 1500 °C-3 h, and (4) 1600 °C-3 h. (b) XRD patterns, showing the process of phase formation of $Dy_{5.5}MoO_{11.25}$ after heat treatment of the mechanically activated oxide mixture under various conditions: (1) 900 °C-4 h, (2) 1100 °C-4 h, (3) 1200 °C-3 h, (4) 1500 °C-3 h, and (5) 1600 °C-3 h.

annealing at 1600 °C because of the partial reduction of the material.

$Ln_{6-x}MoO_{12-\delta}$ (Ln = Dy, Ho, Er, Tm, Yb, Lu; $x = 0, 0.5$) formation from mechanically activated precursors

Fig. 4a and b show XRD patterns illustrating the phase formation process in Dy_6MoO_{12} and $Dy_{5.5}MoO_{11.25}$. Annealing at 900 °C leads to the formation of metastable bixbyite ($Ia\bar{3}$), tetragonal, and rhombohedral (tracks) phases (Fig. 4a and b, scans 1). Annealing at 1200 °C also yields a mixture of a bixbyite, a tetragonal, and a rhombohedral phase (tracks) (Fig. 4a and b, scans 2 and 3, respectively). High-temperature annealing, at 1500 °C of $Dy_6MoO_{12-\delta}$ (Fig. 4a, scan 3) and at 1600 °C of $Dy_{5.5}MoO_{11.25-\delta}$ (Fig. 4b, scan 5), leads to the formation of a pure fluorite ($Fm\bar{3}m$) phase. After annealing at 1600 °C, the $Dy_6MoO_{12-\delta}$ sample contains impurities (Fig. 4a, scan 4), in contrast to $Dy_{5.5}MoO_{11.25-\delta}$ (Fig. 4b, scan 5). The Dy-containing samples with the fluorite structure have a non-uniform coloration (with black inclusions). The samples with the bixbyite structure have a more uniform coloration.

Fig. 5a and b present XRD patterns illustrating the phase formation process in Ho_6MoO_{12} and $Ho_{5.5}MoO_{11.25}$. Here, low-temperature (~900–1100 °C) annealing also leads to the formation of a mixture of a metastable bixbyite phase ($Ia\bar{3}$), a tetragonal, and a rhombohedral phase (tracks) (Fig. 5a and b, scan 1; Fig. 1b, scan 8). After heat treatment at 1600 °C, $Ho_6MoO_{12-\delta}$ has the bixbyite structure ($Ia\bar{3}$) and $Ho_{5.5}MoO_{11.25-\delta}$ has the fluorite structure ($Fm\bar{3}m$). The Ho-containing samples with the fluorite structure also have a non-uniform coloration, which seems to be evidence of partial reduction.

In the case of Er_6MoO_{12} (Fig. 6a), at 900 °C we observe the formation of a metastable bixbyite ($Ia\bar{3}$) phase mixed with a rhombohedral phase (tracks) (Fig. 6a, scan 1). Above 1200 °C,

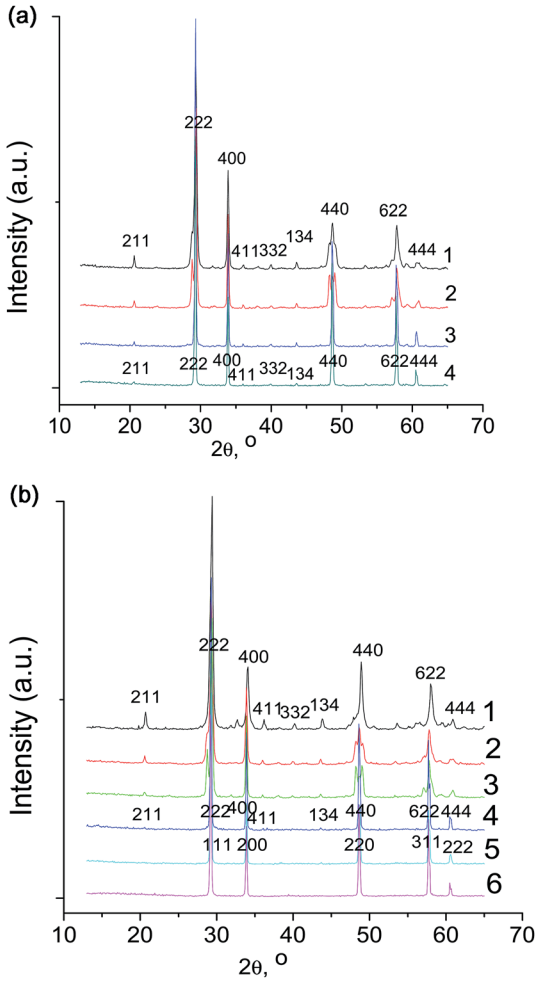

Fig. 5 (a) XRD patterns, demonstrating the process of phase formation of Ho_6MoO_{12} after heat treatment of the mechanically activated oxide mixture at the different temperatures: (1) 1100 °C-4 h, (2) 1200 °C-3 h, (3) 1400 °C-3 h, and (4) 1600 °C-3 h. (b) XRD patterns, demonstrating the process of phase formation of $Ho_{5.5}MoO_{11.25}$ after heat treatment of the mechanically activated oxide mixture at the different temperatures: (1) 900 °C-4 h, (2) 1100 °C-4 h, (3) 1200 °C-3 h, (4) 1400 °C-3 h, (5) 1500 °C-3 h, and (6) 1600 °C-3 h.

we also obtain a mixture of a bixbyite and a rhombohedral phase (tracks) (Fig. 6a, scan 2). Heat treatment at 1400 °C yields well-crystallized rhombohedral Er_6MoO_{12} (Fig. 6a, scan 3), which transforms almost completely into a bixbyite phase at 1500 °C (Fig. 6a, scan 4). At 1600 °C, we obtain a well-crystallized high-temperature bixbyite ($Ia\bar{3}$) phase $Er_6MoO_{12-\delta}$ (Fig. 6a, scan 5). Fig. 6b compares the XRD patterns of $Er_6MoO_{12-\delta}$ and $Er_{5.5}MoO_{11.25-\delta}$ after annealing at 1600 °C. The former material has the bixbyite structure ($Ia\bar{3}$) and the latter has the fluorite ($Fm\bar{3}m$) structure. To examine the influence of annealing time on the phase formation process at a low temperature (1200 °C), the mechanically activated mixture of the oxides $3Er_2O_3 + MoO_3$ was sintered at 1200 °C for 4 and 40 h, respectively (Fig. 6c). We observed the formation of an $Er_6MoO_{12-\delta}$ bixbyite cubic phase (metastable) (Fig. 6c, scan 1) in the thermodynamic stability region of the rhombohedral ($R\bar{3}$) Er_6MoO_{12} phase with the same composition under the effect of kinetic factors.[19] The transformation into the stable rhombohedral ($R\bar{3}$) Er_6MoO_{12} phase can be induced by a longer heating duration (Fig. 6c, scan 2). This is a kinetic (growth-related) transition from metastable bixbyite to the stable rhombohedral ($R\bar{3}$) Er_6MoO_{12} at 1200 °C. A similar process (from metastable fluorite to the stable rhombohedral ($R\bar{3}$)) was recently reported as an irreversible, first order diffusional ordering process for the Ln_6WO_{12} (Ln = Y, Ho, Er, Yb).[29]

Yb_6MoO_{12} and $Yb_{5.5}MoO_{11.25}$ have identical phase formation sequences (Fig. 7a and b). A metastable bixbyite phase ($Ia\bar{3}$) is formed at 900 °C (Fig. 7a and b, scans 1). The stability range of the rhombohedral ($R\bar{3}$) phase, 1200 to 1500 °C, is broader in comparison with that of Er_6MoO_{12} (Fig. 7a, scans 2–4; Fig. 7b, scans 3–5). After annealing at 1600 °C, both $Yb_6MoO_{12-\delta}$ and $Yb_{5.5}MoO_{11.25-\delta}$ have the high-temperature bixbyite structure ($Ia\bar{3}$) (Fig. 7a and b, scans 5 and 6, respectively). Thus, Ho, Er, and Yb molybdates are characterized by the formation of a metastable bixbyite phase below 1000 °C, and at high temperatures we observe order–disorder (rhombohedral–bixbyite) phase transitions for Ln_6MoO_{12} (Ln = Er, Yb).

Tm_6MoO_{12} was also found to undergo an order–disorder (rhombohedral–bixbyite) phase transition, like Ln_6MoO_{12} (Ln = Er, Yb) (Fig. 8, scans 1 and 2). At the same time, Lu_6MoO_{12} seems to undergo an order–disorder transition at higher temperatures, like $La_{5.5}MoO_{11.25}$, as evidenced by the fact that, in the range 1400–1600 °C, Lu_6MoO_{12} retains the rhombohedral structure (Fig. 8, scans 3 and 4). A metastable fluorite phase ($Fm\bar{3}m$) was obtained previously for Lu_6MoO_{12} in the range 800–1000 °C using a wet-chemical method.[6] It seems likely that above 1600 °C this compound exists as a high-temperature fluorite phase, rather than as a bixbyite phase.

Thus, in this study, Ln_6MoO_{12} (Ln = Er, Yb, Tm) and solid solutions based on these compounds were shown for the first time to undergo high-temperature order–disorder (rhombohedral–bixbyite) phase transitions ($T_{PT} \geq 1500$ °C), and we identified metastable bixbyite phases forming below 1000 °C.

Morphotropic and thermodynamic order–disorder (fluorite–rhombohedral phase–bixbyite) transitions

Fig. 9 shows the unit-cell parameter a as a function of the Ln ionic radius of the $Ln_{5.5}MoO_{11.25-\delta}$ (Ln = Er–Gd) molybdates with the fluorite structure after annealing at 1600 °C. The a cell parameter is seen to rise linearly with the Ln ionic radius. Also shown in Fig. 9 is the a cell parameter of the metastable fluorite phase $La_{5.5}MoO_{11.25-\delta}$ synthesized at 900 °C. Fitting the dependence of a on the Ln ionic radius of the $Ln_{5.5}MoO_{11.25-\delta}$ (Ln = Er–Gd) molybdates at 1600 °C by a straight line, we find that the a of high-temperature $La_{5.5}MoO_{11.25}$ markedly exceeds that of metastable fluorite $La_{5.5}MoO_{11.25}$.

The data in Fig. 10 illustrate the morphotropic fluorite–bixbyite phase transition in the $Ln_6MoO_{12-\delta}$ molybdates after annealing at 1600 °C for 3 h. Fig. 10 and Table 1 present the unit-cell parameter as a function of the Ln^{3+} ionic radius of $Ln_6MoO_{12-\delta}$ (Ln = Yb, Tm, Er, Ho, Dy, Gd). The heavy rare-earth molybdates $Ln_6MoO_{12-\delta}$ (Ln = Ho, Er, Yb, Tm) crystallize in the bixbyite structure ($Ia\bar{3}$) and the intermediate rare-earth

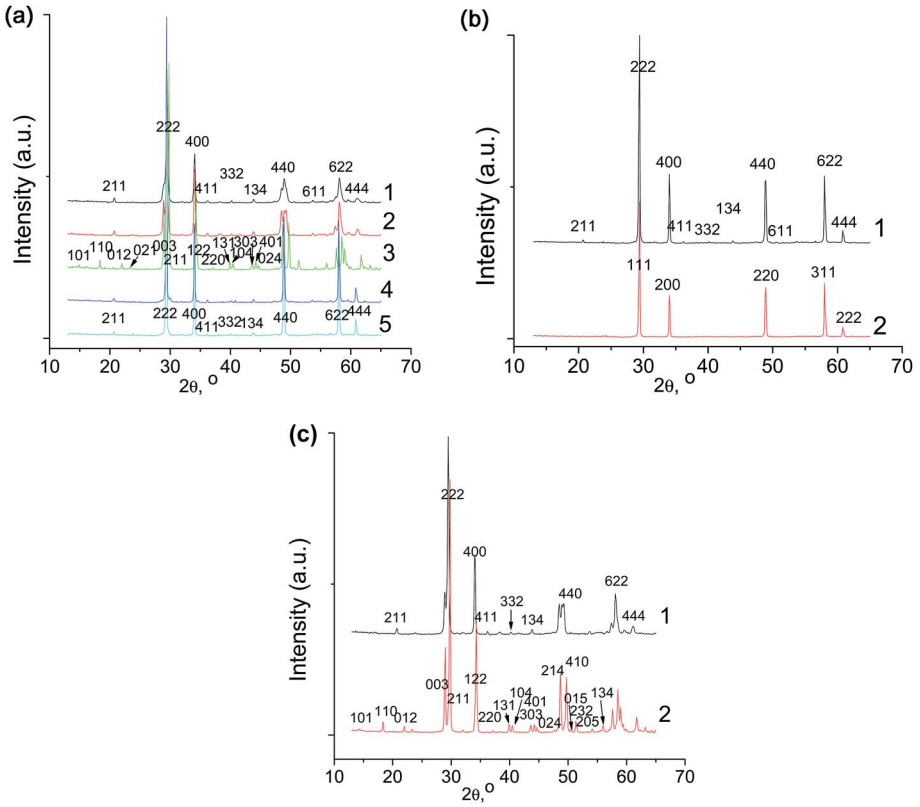

Fig. 6 (a) XRD patterns, showing the process of phase formation of Er_6MoO_{12} after heat treatment of the mechanically activated oxide mixture under various conditions: (1) 1100 °C-4 h, (2) 1200 °C-3 h, (3) 1400 °C-3 h, (4) 1500 °C-3 h, and (5) 1600 °C-3 h. (b) XRD patterns of the (1) $Er_6MoO_{12-\delta}$ ($Ia\bar{3}$) and (2) $Er_{5.5}MoO_{11.25}$ ($Fm\bar{3}m$), synthesized at 1600 °C-3 h. (c) XRD patterns of the Er_6MoO_{12} after thermal annealing at 1200 °C for (1) 4 h and (2) 40 h.

molybdates $Ln_6MoO_{12-\delta}$ (Ln = Dy, Gd) crystallize in the fluorite structure ($Fm\bar{3}m$). The $Ho_{6-x}MoO_{12-\delta}$ (x = 0, 0.5) molybdates were shown to exist in two phases, with the fluorite and bixbyite structures, and the heavy rare-earth molybdates Ln_6MoO_{12} (Ln = Er, Tm, Yb) exist as rhombohedral and bixbyite phases.

Fig. 11 plots the unit-cell parameters against the Ln^{3+} ionic radius of rhombohedral Ln_6MoO_{12} (Ln = Er, Tm, Yb, Lu) prepared at 1400 °C (3 h). Both a and c increase with the Ln^{3+} ionic radius. Note that the temperature stability range of the rhombohedral phase increases with decreasing Ln^{3+} ionic radius. In particular, the rhombohedral phase of Er_6MoO_{12} exists only after a short 3 h annealing at 1400 °C, whereas that of $Yb_{6-x}MoO_{12-\delta}$ (x = 0, 0.5) exists after annealing in the range 1200–1500 °C (Table 1; Fig. 7a and b). However the true stability region of the Er_6MoO_{12} rhombohedral phase starts from 1200 °C as shown by long temperature annealing (40 h) at 1200 °C (Fig. 6c, scan 2). Rhombohedral ($R\bar{3}$) Tm_6MoO_{12} also exists below 1600 °C (Table 1; Fig. 8). The rhombohedral phase of Lu_6MoO_{12} persists at 1600 °C, and it seems to undergo disordering at a higher temperature.

In this study, using brief annealing (3 h) of mechanically activated oxide mixtures, we were able to obtain high-temperature bixbyite $Ln_6MoO_{12-\delta}$ (Ln = Ho, Er, Tm, Yb) in the range 1400 to 1600 °C. The stability of the heaviest rare-earth molybdates and tungstates, $Ln_6Mo(W)O_{12}$ (Ln = Tm, Yb, Lu), was studied qualitatively by Aitken *et al.*[27] and was shown to be even higher than that of Ln_2O_3 (Ln = Tm, Yb, Lu).

Microanalysis data of the Ln and Mo-containing samples synthesized in this work are presented in Table 2. These results suggest that no considerable molybdenum loss occurred in the samples during short high-temperature annealing in the range 1200–1600 °C. These results agree with data of rhombohedral R_6MoO_{12} (R = Tm–Lu, Y).[27] It is worth noting, however, that the accuracy of determining the Ln/Mo ratio by EDX spectroscopy decreases with increasing synthesis temperature and is lower for the heavy rare-earth molybdates in comparison with the light and intermediate rare-earth molybdates. Note also that the accuracy of determining the Ln/Mo ratio is not very high in the case of the mixed-phase samples synthesized at 1200 °C (Table 2, samples A and B). The data in Fig. 12 illustrate the Mo distribution over the $Yb_6MoO_{12-\delta}$ (Table 2, no. 23) (Fig. 12a and b) and $Ho_6MoO_{12-\delta}$ (Table 2, no. 10) (Fig. 12c and d) samples synthesized at 1600 °C. The Mo is seen to be evenly distributed throughout the samples. Similar data were obtained for all of the samples, independent of the synthesis temperature.

Given this, using mechanochemical synthesis, we were able to produce rather dense ceramics with fluorite and related (rhombohedral ($R\bar{3}$) and bixbyite ($Ia\bar{3}$)) structures, and it is of obvious interest to study not only the structure but also the electrical properties of these polymorphs. Indeed, as shown

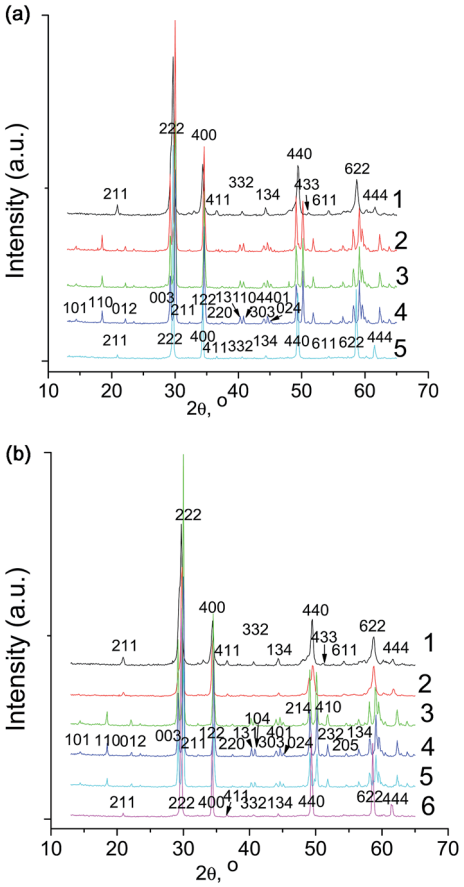

Fig. 7 (a) XRD patterns, demonstrating the process of phase formation of Yb_6MoO_{12} after heat treatment of the mechanically activated oxide mixture at the different temperatures: (1) 900 °C-4 h, (2) 1200 °C-4 h, (3) 1400 °C-3 h, (4) 1500 °C-3 h, and (5) 1600 °C-3 h. (b) XRD patterns, demonstrating the process of phase formation of $Yb_{5.5}MoO_{11.25}$ after heat treatment of the mechanically activated oxide mixture at the different temperatures: (1) 900 °C-4 h, (2) 1100 °C-4 h, (3) 1200 °C-4 h, (4) 1400 °C-3 h, (5) 1500 °C-3 h, and (6) 1600 °C-3 h.

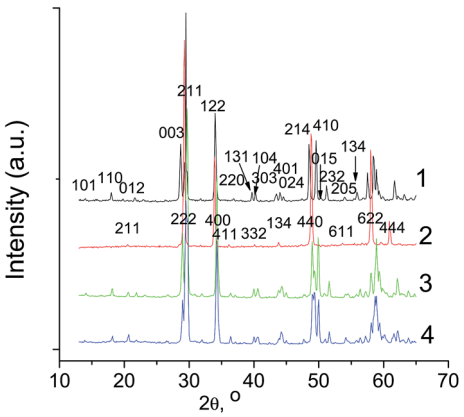

Fig. 8 XRD patterns of Tm_6MoO_{12} and Lu_6MoO_{12}, synthesized (1 and 3) at 1400 °C-3 h and (2 and 4) at 1600 °C-3 h.

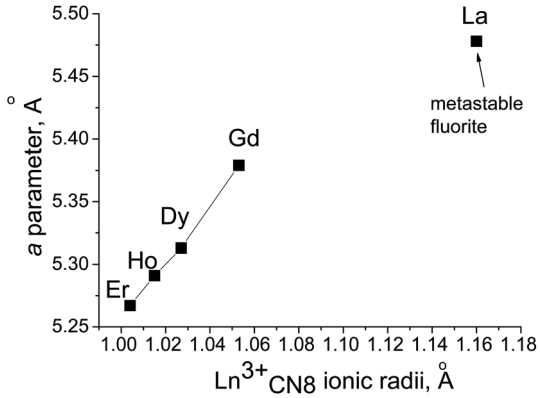

Fig. 9 Unit-cell parameter as a function of the Ln^{3+} ionic radius of fluorite $Ln_{5.5}MoO_{11.25}$ (Ln = Er–Gd) after annealing at 1600 °C for 3 h.

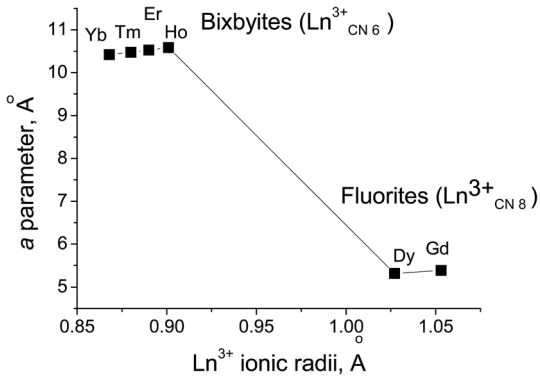

Fig. 10 Fluorite–bixbyite morphotropic transition in $Ln_6MoO_{12-\delta}$ after annealing at 1600 °C for 3 h: unit-cell parameter as a function of the Ln^{3+} ionic radius of $Ln_6MoO_{12-\delta}$ (Ln = Yb, Er, Ho, Dy, Gd).

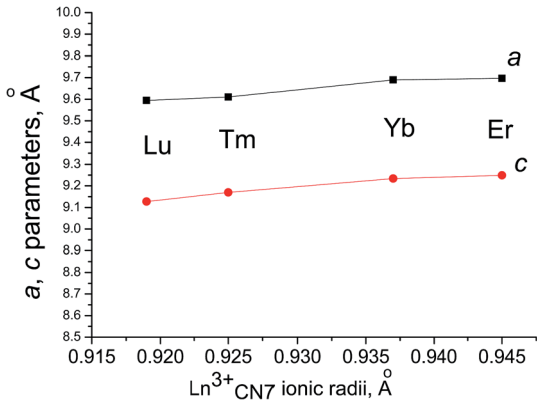

Fig. 11 Unit-cell parameters as functions of the Ln^{3+} ionic radius of rhombohedral ($R\bar{3}$) Ln_6MoO_{12} (Ln = Er, Tm, Yb, Lu) prepared at 1400 °C (3 h).

earlier, $La_{5.8}Zr_{0.2}MoO_{12.1}$ and $Ln_{6-x}Zr_xMoO_{12+\delta}$ (Ln = Nd, Sm, Dy; $x = 0.6$) zirconium-doped materials have oxygen ion conductivity in a dry atmosphere and proton conductivity in a wet atmosphere below 700, 500, and 425 °C.[10,11] These materials have ionic conductivity at low and medium temperatures, whereas at higher temperatures electronic conductivity prevails. Thus, it is important to evaluate the conductivity of the zirconium-free $Ln_{6-x}MoO_{12-\delta}$ (Ln = La, Yb; $x = 0$, 0.5)

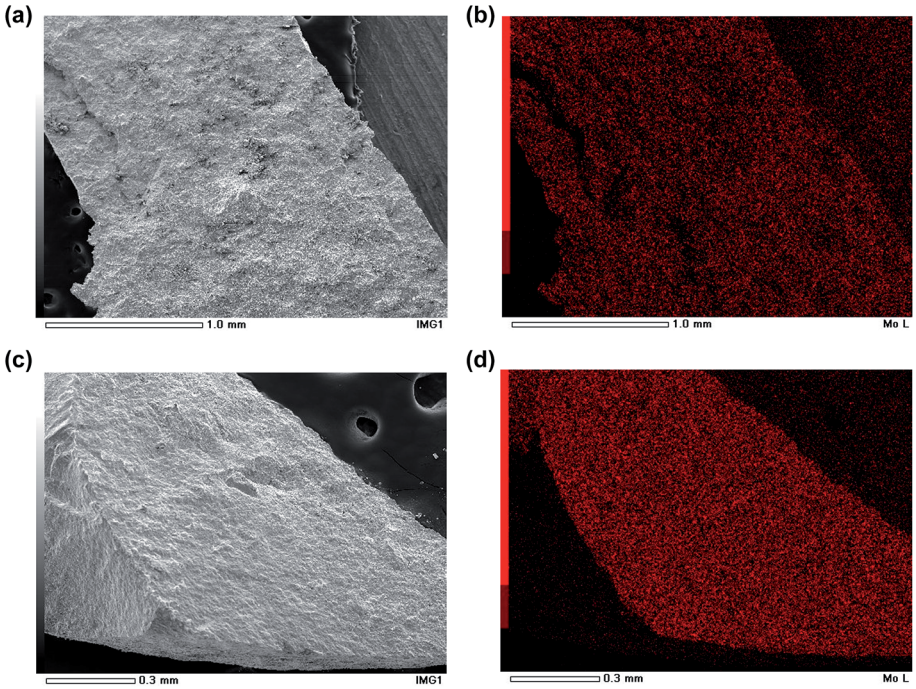

Fig. 12 (a and c) SEM image and (b and d) Mo X-ray map of $Yb_6MoO_{12-\delta}$ and $Ho_6MoO_{12-\delta}$, respectively, synthesized at 1600 °C.

rare-earth molybdates with the rhombohedral and bixbyite structures.

Total conductivity of $La_{5.5}MoO_{11.25}$ in dry and wet air

The impedance spectra obtained for the rhombohedral $La_{5.5}MoO_{11.25}$ ($T_{syn.} = 1600$ °C) in dry and wet air are given in Fig. 13. In the low-temperature range the spectra showed two separate semicircles that were attributed to the sample bulk and electrode polarization. The values of the equivalent specific bulk and electrode capacitances extracted *via* non-linear least squares fitting ($C_b \sim 10^{-12}$ F cm^{-1} and $C_{el} \sim 10^{-5}$ F cm^{-2}) are consistent with the aforementioned interpretation. Fig. 14 presents the total conductivity of $La_{5.5}MoO_{11.25}$ ($T_{syn.} = 1600$ °C) in dry and wet air extracted from these data (Fig. 13). An increase of total conductivity in wet air as compared to the conductivity in dry air is indicative of hydration of this sample resulting in proton conductivity. The Arrhenius plot of the conductivity of $La_{5.5}MoO_{11.25}$ shows an inflection point at ~600 °C in a wet atmosphere. A shift from predominant proton conduction at low temperature to predominant electron conduction in the high temperature range takes place. As far as the conductivity of $La_{5.5}MoO_{11.25}$ in dry air is concerned, we believe that a small amount of residual water might have caused a slight increase in conductivity at the lowest temperatures (below 200 °C). The marginal change of slope at ~600 °C is probably related to the onset of oxygen ion conductivity as the concentration of protons is very low under dry air. The activation energies for conduction in this sample below and above 600 °C are indicated in Table 3.

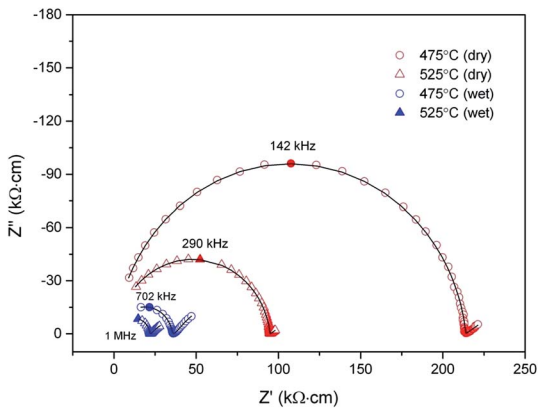

Fig. 13 Impedance spectra of rhombohedral $La_{5.5}MoO_{11.25}$ ($T_{syn.} = 1600$ °C) in dry air and wet air at difference temperatures.

Even though the conductivity of $La_{5.5}MoO_{11.25}$ (2×10^{-4} at 600 °C) is lower than that of $La_{6-x}WO_{12-\delta}$,[7–9] the more complex structure of $La_{5.5}MoO_{11.25}$ seems to ensure higher stability of this compound in a reducing atmosphere.[30] Particular features of its microstructure may also play a role.[31]

Total conductivity of two Yb_6MoO_{12} polymorphs: bixbyite ($Ia\bar{3}$) and rhombohedral ($R\bar{3}$) in dry and wet air

Fig. 15 shows the typical impedance spectra of bixbyite $Yb_6MoO_{12-\delta}$ ($Ia\bar{3}$) at low temperatures (480 and 525 °C, Fig. 15a) and at higher temperatures (650 and 700 °C, Fig. 15b). The spectra each consist of two arcs of circles and can be described using an equivalent circuit consisting of two series connected elements, each composed of a parallel connected resistance (R) and constant phase element (CPE). The impedance of the constant phase element can be represented as

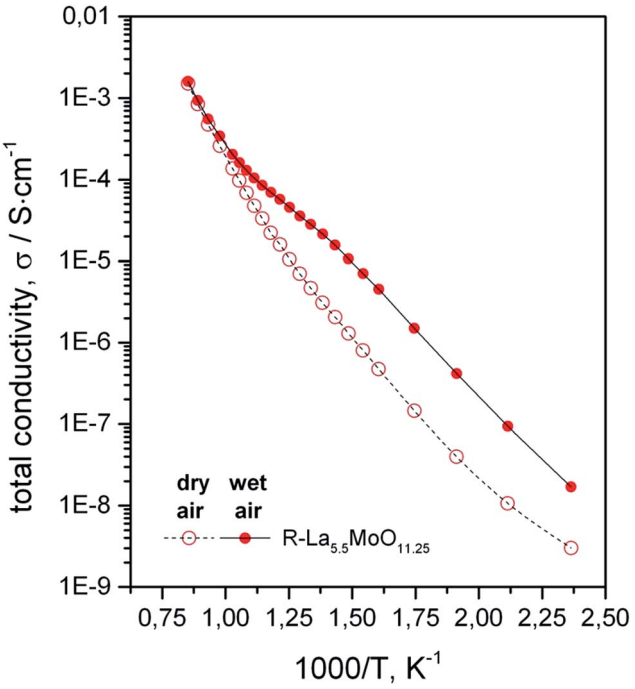

Fig. 14 Arrhenius plots of the total conductivity of $La_{5.5}MoO_{11.25}$ in dry and wet air.

$$Z_{CPE} = \frac{1}{A(j\omega)^P}$$

where A is a proportionality factor and the exponent P is related to the phase angle.

The real-axis intercept of the high-frequency arc is the bulk resistance of the material, R_{bulk}. Note that the center of the high-frequency arc is slightly depressed relative to the real axis (the exponent P is near 0.9). This behavior may be caused by inductive interferences in the tubular furnace used in our measurements. The apparent capacitance (A) is $\sim 10^{-11}$ F cm^{-1}, which corresponds to the geometric capacitance of the material. The other arc (at medium and low frequencies) represents the contribution of electrode polarization at the electrode/electrolyte interface to the impedance response of the system. Note that R_{bulk} decreases with increasing air humidity (Fig. 15a). This points to proton conductivity, whose contribution to the total conductivity of the material increases with decreasing temperature.

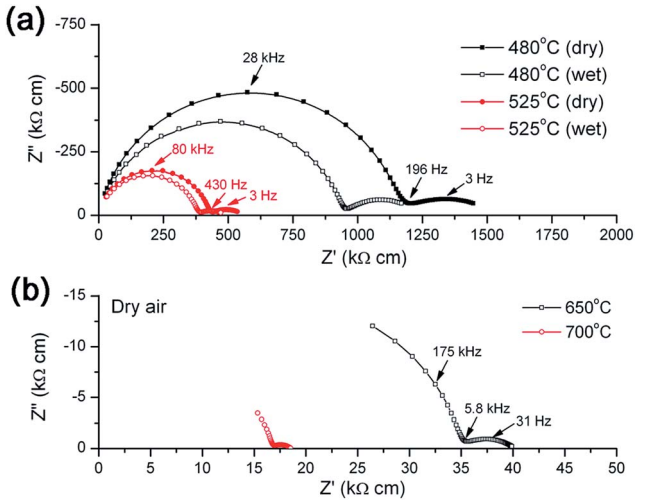

Fig. 15 Impedance spectra of bixbyite $Yb_6MoO_{12-\delta}$ ($Ia\bar{3}$) ($T_{syn.} = 1600$ °C) in dry and wet air.

Fig. 16 shows the typical impedance spectra of rhombohedral ($R\bar{3}$) Yb_6MoO_{12} at low (525 and 570 °C) (Fig. 16a) and higher (650 and 700 °C) (Fig. 16b) temperatures. In contrast to the spectrum of $Yb_6MoO_{12-\delta}$ with the bixbyite structure ($Ia\bar{3}$), the impedance response of this system consists of one arc of a circle, which can be represented by an equivalent circuit composed of a parallel connected resistance (R) and constant phase element (CPE). The real-axis intercept is the bulk resistance of the material. Note that the center of the arc is also slightly depressed relative to the real axis (the exponent P is near 0.8). The apparent capacitance (A) of the material is also $\sim 10^{-11}$ F cm^{-1}.

Fig. 17 presents the temperature dependency of the total conductivity of $Yb_6MoO_{12-\delta}$ ($Ia\bar{3}$) and Yb_6MoO_{12} ($R\bar{3}$) in dry and wet air. An increase of total conductivity in wet air as compared to the conductivity in dry air is indicative of hydration of $Yb_6MoO_{12-\delta}$ bixbyite at $T < 600$ °C resulting in proton conductivity (Fig. 17, curves 1 and 2). Above 600 °C, the electronic conductivity increases, which is accompanied by changes in activation energy (Table 3). Above 600 °C, bixbyite $Yb_6MoO_{12-\delta}$ has mixed conductivity. Rhombohedral ($R\bar{3}$) Yb_6MoO_{12} has no proton conductivity below 600 °C and seems to be an oxygen ion conductor in dry air ($E_a = 0.53$–0.58 eV) (Table 3). The activation energy for oxygen ion conduction typically falls in the range 0.6–1 eV. However, a number of oxygen ion conductors have lower

Table 3 Activation energy for bulk conduction in the solid solutions in dry and wet air

	Activation energy of bulk conductivity E_a, eV in dry air		Activation energy of bulk conductivity E_a, eV in wet air	
Composition	Below 600 °C	Above 600 °C	Below 600 °C	Above 600 °C
$La_{5.5}MoO_{11.25}$	0.71	1.3	0.68	1.15
$Yb_6MoO_{12-\delta}$ bixbyite ($Ia\bar{3}$)	1.16	1.37	1.07	1.32
Yb_6MoO_{12} rhombohedral ($R\bar{3}$)	0.53	0.98	0.58	0.98

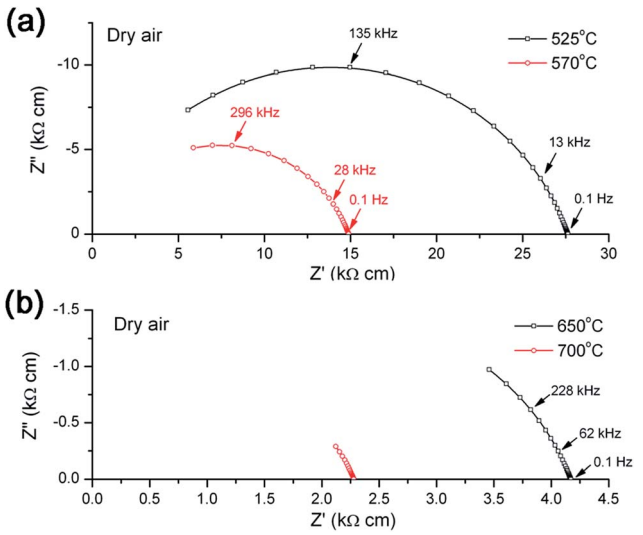

Fig. 16 Impedance spectra of rhombohedral Yb_6MoO_{12} ($R\bar{3}$) ($T_{syn.}$ = 1500 °C) in dry and wet air.

activation energies. For example, as shown by Kiruthika *et al.*[32] some pyrochlore-structured compounds have lower activation energies for bulk conduction. In particular, the activation energy for bulk conduction in $Gd_{1.8}Sr_{0.2}Hf_2O_{6.9}$ and $Nd_{1.9}Sr_{0.1}Hf_2O_{6.95}$ is 0.57 and 0.42 eV, respectively.

At T > 600 °C the activation energy of rhombohedral ($R\bar{3}$) Yb_6MoO_{12} conductivity is E_a = 0.98 eV (Table 3) and we can suppose that ionic conductivity contribution prevails in rhombohedral ($R\bar{3}$) Yb_6MoO_{12} at these temperatures.

As shown earlier, the proton conductivity of zirconium-doped molybdates decreases markedly with decreasing Ln ionic radius.[10] The highest proton conductivity is offered by the La- and Nd-containing solid solutions. With decreasing ionic radius across the lanthanide series, the proton contribution to the total conductivity decreases, and $Dy_{5.4}Zr_{0.6}MoO_{12.3}$ has

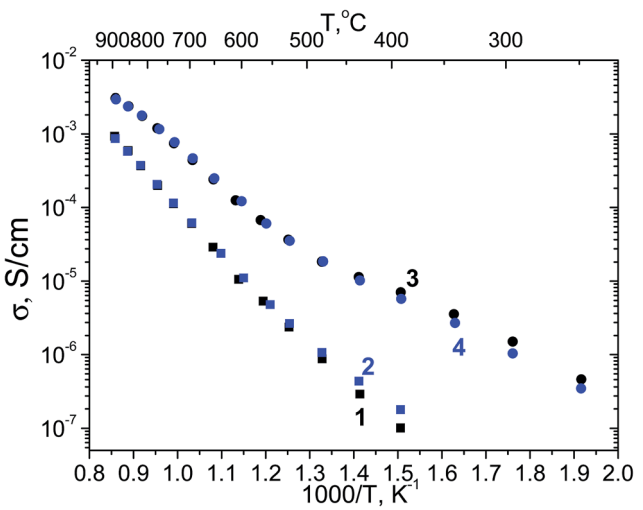

Fig. 17 Arrhenius plots of the total conductivity in (1 and 3) dry and (2 and 4) wet air of two Yb_6MoO_{12} polymorphs: (1 and 2) bixbyite ($Ia\bar{3}$) $Yb_6MoO_{12-\delta}$ and (3 and 4) rhombohedral ($R\bar{3}$) Yb_6MoO_{12}.

insignificant proton conductivity.[10] The Arrhenius plot of the conductivity of rhombohedral ($R\bar{3}$) Yb_6MoO_{12} has a characteristic break at 550 °C (Fig. 17, curves 3 and 4). In previous studies of zirconium-doped rare-earth molybdates and tungstates, such breaks were interpreted as evidence of a change in the dominant carrier type.[7,10] In a dry atmosphere at low temperatures (below 550 °C), charge transport is mainly due to oxygen ions, whereas at high temperatures electrons and holes prevail at low and high oxygen partial pressures, respectively. Rhombohedral ($R\bar{3}$) Yb_6MoO_{12} seems to have purely oxygen ion conductivity in wet air below 550 °C (Table 3), whereas the conductivity of $La_{5.5}MoO_{11.25}$ has a significant proton contribution (Fig. 14). Above 600 °C, both rhombohedral ($R\bar{3}$) and bixbyite $Yb_6MoO_{12-\delta}$ have growing electronic conductivity contribution, which increases with temperature (Table 3).

The total conductivity of rhombohedral ($R\bar{3}$) Yb_6MoO_{12} is more than an order of magnitude higher than the conductivity of $Yb_6MoO_{12-\delta}$ bixbyite, and is 3×10^{-5} S cm^{-1} at 500 °C.

Conclusions

We have investigated the phase formation processes of $Ln_{6-x}MoO_{12-\delta}$ (Ln = La, Gd, Dy, Ho, Er, Tm, Yb, Lu; x = 0, 0.5) rare-earth molybdates in the range 900–1600 °C. The materials have been synthesized *via* mechanical activation of oxide mixtures, which ensured the formation of molybdates even during milling. Our data on low-temperature phase formation and crystallization processes in the range 900–1100 °C demonstrate the formation of a metastable fluorite, bixbyite, and tetragonal or rhombohedral phase, depending on the Ln ionic radius.

High-temperature synthesis in the range 1400–1600 °C allowed us to detect for the first time thermodynamic order–disorder (rhombohedral ($R\bar{3}$)–bixbyite ($Ia\bar{3}$)) phase transitions in the heavy rare-earth molybdates $Ln_{6-x}MoO_{12-\delta}$ (Ln = Er, Tm, Yb; x = 0, 0.5). The stability range of the rhombohedral phase increases with decreasing Ln ionic radius.

The total conductivity of $La_{5.5}MoO_{11.2}$ and two Yb_6MoO_{12} polymorphs, with rhombohedral ($R\bar{3}$) and bixbyite ($Ia\bar{3}$) structures, has been determined in dry and wet air using impedance spectroscopy. Below 600 °C, the conductivity of $La_{5.5}MoO_{11.25}$ and bixbyite $Yb_6MoO_{12-\delta}$ ($Ia\bar{3}$) has a significant proton contribution. Rhombohedral ($R\bar{3}$) Yb_6MoO_{12} has oxygen ion conductivity under these conditions (T < 550 °C). At 600 °C in wet air, the conductivity of undoped $La_{5.5}MoO_{11.25}$, which has a complex structure derived from the rhombohedral one, is 2×10^{-4} S cm^{-1}. The conductivity of rhombohedral ($R\bar{3}$) Yb_6MoO_{12} in air at 600 °C is 1×10^{-4} S cm^{-1} and that of bixbyite $Yb_6MoO_{12-\delta}$ at 600 °C is 1×10^{-5} S cm^{-1}. So we have obtained and investigated the first members of oxygen ion- and/or proton-conducting materials with the bixbyite ($Ia\bar{3}$) and rhombohedral ($R\bar{3}$) structure in the family of $Ln_{6-x}MoO_{12-\delta}$ (Ln = Ho, Er, Tm, Yb, Lu; x = 0, 0.5) molybdates.

Acknowledgements

This work was supported by the Russian Foundation for Basic Research (grant no. 16-03-00143). We are grateful to Dr Maxim

Avdeev from the Bragg Institute, Australian Nuclear Science and Technology Organization for useful discussions in preparing the manuscript.

References

1 J. Wang, X. Jing, C. Yan, J. Lin and F. Liao, *J. Lumin.*, 2006, **121**, 57.
2 S. Vishnu, S. Jose and M. L. Reddy, *J. Am. Ceram. Soc.*, 2011, **94**, 997.
3 J. Kumar Kar, R. Stevens and C. R. Bowen, *J. Alloys Compd.*, 2008, **461**, 77.
4 J. Sun, B. Xue and H. Du, *Infrared Phys. Technol.*, 2013, **60**, 10.
5 J. Sun, B. Xue and H. Du, *Opt. Commun.*, 2013, **298–299**, 37.
6 H. Li, H. K. Yang, B. K. Moon, B. C. Choi, J. H. Jeong, K. Jang, H. S. Lee and S. S. Yi, *Inorg. Chem.*, 2011, **50**(24), 12522.
7 C. Solís, S. Escolástico, R. Haugsrud and J. M. Serra, *J. Phys. Chem. C*, 2011, **115**, 11124.
8 A. Magrasó and R. Haugsrud, *J. Mater. Chem. A*, 2014, **2**, 12630.
9 G. S. Partin, D. V. Korona, A. Ya. Neiman and K. G. Belova, *Russ. J. Electrochem.*, 2015, **51**, 381.
10 S. N. Savvin, A. V. Shlyakhtina, A. B. Borunova, L. G. Shcherbakova, J. C. Ruiz-Morales and P. Núñez, *Solid State Ionics*, 2015, **271**, 91.
11 S. N. Savvin, A. V. Shlyakhtina, I. V. Kolbanev, A. V. Knotko, D. A. Belov, L. G. Shcherbakova and P. Nuñez, *Solid State Ionics*, 2014, **262**, 713.
12 K. Kuribayashi, M. Yoshimura, T. Ohta and T. Sata, *J. Am. Ceram. Soc.*, 1980, **63**, 644.
13 M. Foex, *Bull. Soc. Chim. Fr.*, 1967, **10**, 3696.
14 M. Yoshimura, J. Ma and M. Kakihana, *J. Am. Ceram. Soc.*, 1998, **10**, 2721.
15 D. Schildhammer, G. Fuhrmann, L. L. Petschnig, S. Penner, M. Kogler, T. Gotsch, A. Scaur, N. Weinberger, A. Saxer, H. Schottenberger and H. Huppertz, *Chem. Mater.*, 2016, **28**(20), 7487.
16 S. Escolastico, V. B. Vert and J. M. Serra, *Chem. Mater.*, 2009, **21**, 3079.
17 V. M. Goldschmidt, *Usp. Fiz. Nauk*, 1929, **6**, 811.
18 G. M. Kuz'micheva, *Basic Crystal-Chemical Concepts*, MITKhT, Moscow, 2001.
19 A. G. Shtukenberg, Yu. O. Punin and O. V. Frank-Kamenetskaya, *Usp. Khim.*, 2006, **75**(12), 1212.
20 A. A. Chernov, *Usp. Fiz. Nauk*, 1970, **100**(2), 277.
21 A. A. Chernov, Kinetic phase transitions, *Soviet Physics–JETP*, 1968, **26**(6), 1182–1186.
22 A. V. Shlyakhtina, *Crystallogr. Rep.*, 2013, **58**, 545.
23 V. V. Popov, A. P. Menushenkov, A. A. Yaroslavtsev, Ya. V. Zubavichus, B. R. Gaynanov, A. A. Yastrebtsev, D. S. Leshchev and R. V. Chernikov, *J. Alloys Compd.*, 2016, **689**, 669.
24 V. M. Vidojikovic, A. R. Brankovic and R. B. Petronijevic, *Mater. Lett.*, 1996, **28**, 59.
25 A. F. Fuentes, K. Boulahya, M. Maczka, J. Hanuza and U. Amador, *Solid State Sci.*, 2005, **7**, 343.
26 ICDD PDF 24-1087. Mcllvried, McCarthy, Penn State University, University Park, Pennsylvania, USA. 1972.
27 E. A. Aitken, S. F. Bartram and E. F. Juenke, *Inorg. Chem.*, 1964, **3**, 949.
28 M. Amsif, A. Magraso, D. Marrero-Lopez, J. C. Ruiz-Morales, J. Canales-Vazquez and P. Nuñez, *Chem. Mater.*, 2012, **24**, 3868.
29 Z. D. Apostolov, P. Sarin, R. P. Haggerty and W. M. Kriven, *J. Am. Ceram. Soc.*, 2013, **96**, 987.
30 J. S. Mohammed, The Degree Master of Science in Materials Science and Engineering, Georgia Institute of Technology, 2004.
31 A. V. Shlyakhtina, S. N. Savvin, A. V. Knotko, L. G. Shcherbakova and P. Nuñez, *Inorg. Mater.*, 2016, **52**, 1055.
32 G. V. M. Kiruthika, K. V. Gavindan Kutty and U. V. Varadarju, *Solid State Ionics*, 1998, **110**, 335.

